Erschienen in: Physical Review Letters ; 121 (2018), 9. - 094801
https://dx.doi.org/10.1103/PhysRevLett.121.094801

Tilted electron pulses

Dominik Ehberger[1,2], Andrey Ryabov[1,2] and Peter Baum[1,2,*]

[1]*Ludwig-Maximilians-Universität München, Am Coulombwall 1, 85748 Garching, Germany*
[2]*Max-Planck-Institute of Quantum Optics, Hans-Kopfermann-Str. 1, 85748 Garching, Germany*
**peter.baum@lmu.de*

We report the all-optical generation and characterization of tilted electron pulses by means of single-cycle terahertz radiation at an electron-transmitting mirror at slanted orientation. Femtosecond electron pulses with chosen tilt angle are produced at almost arbitrary target location. The experiments along with theory further reveal that pulse front tilt in electron optics is directly connected to angular dispersion. Quantum mechanical considerations suggest that this relation is general for particle beams at any degree of coherence. These results indicate that ultrashort electron pulses can be shaped in space and time as versatilely as femtosecond laser pulses, but at 10^5 times finer wavelength and sub-nm imaging resolution.

Ultrashort electron pulses allow the direct visualization of atomic and electronic motion during matter transformations in space and time. For generating the necessary few-femtosecond and attosecond electron pulses, technology is currently progressing from microwave electronics to an all-optical control regime, where the optical cycles of laser-generated radiation are used to steer the electrons in a direct and jitter-free way, obviating the need for active synchronization electronics. So far, ultrashort electron pulses have been accelerated [1], compressed [2,3], energy-modulated [4] and streaked [2,5] by all-optical approaches, but many applications require more complex phase-space correlations involving multiple dimensions.

Here we report a multidimensional, dynamical control of electron pulses by all-optical means, exemplified by the generation and characterization of tilted electron pulses. Such pulses, propagating non-normally to their pulse front, promise to improve free-electron laser performance [6] and enable pump-probe experiments in which optical cycles are used for sample excitation [7,8].

Our concept (Fig. 1a) is based on the controlled phase space modulation of a beam of electrons (blue) by the cycles of electromagnetic radiation (red). The interaction is mediated by an ultrathin metal mirror (dark grey) in an off-angle geometry. Electrons can pass through, but radiation is reflected. The electrons therefore obtain a net momentum change from the optical cycles due to their passage through the mirror material within sub-cycle time [9]. For generating tilted electron pulses with multidimensional correlations in space and time, we place the mirror in such a way in the optical beam that different lateral slices of the electron beam are accelerated or decelerated with a linear gradient across the beam. Simultaneously, we ensure that the entire beam is uniformly compressed in time [2]. Therefore, we expect ultrashort and tilted pulses on a target after free-space propagation.

In order to find the appropriate geometry, we treat the electron beam classically and assume a point charge e of initial velocity $v_\mathrm{e} = \beta c$ along the z-axis (initial momentum p_z and $p_y = 0$) that is passing through a perfect mirror ($y = z = 0$) irradiated with a p-polarized plane-wave (angular frequency ω, peak field strength E_0 at $y = z = t = 0$) as an approximation for the fields in the waist of a Gaussian beam (full width at half maximum w_0, Rayleigh range z_R; $z_R \gg w_0$). The mirror reflection causes a moving interference pattern with magnetic and electric contributions. An analytic derivation (see supplementary) provides the sideways/longitudinal momentum transfer components Δp_y and Δp_z after the interaction:

$$\Delta p_{y,z}(t) = eE_0 \, A_{y,z}(\theta_e, \theta_{THz}, \beta) \, \frac{\sin(\omega t)}{\omega}. \qquad (1)$$

Here, *t* is the arrival time of the electron at the mirror. The amplitude of this sinusoidal momentum modulation depends on the angles θ_e and θ_{THz} (see Fig. 1b) via the geometry factors

$$A_y = \pm\left(\frac{\cos(\theta_e + \theta_{THz}) + \beta}{1 + \beta\cos(\theta_e + \theta_{THz})} - \frac{\cos(\theta_\mathrm{e} - \theta_{THz}) - \beta}{1 - \beta\cos(\theta_e - \theta_{THz})}\right), \qquad (2)$$

$$A_z = \pm\left(\frac{\sin(\theta_\mathrm{e} - \theta_{THz})}{1 - \beta\cos(\theta_e - \theta_{THz})} - \frac{\sin(\theta_e + \theta_{THz})}{1 + \beta\cos(\theta_e + \theta_{THz})}\right), \qquad (3)$$

where the positive/negative sign is for same/opposite incidence of the electrons and the plane-wave with respect to the mirror. The momentum gain is assumed to be small compared to the initial momentum ($\Delta p_{y,z} \ll p_z$) and ponderomotive effects are neglected. Under these assumptions, Eq. 1-3 hold for relativistic particles, too.

We find that acceleration and deflection are in phase with each other, regardless of the angles. Furthermore, both momentum changes are phase-shifted by $\pi/2$ with respect to the incident electromagnetic wave. Therefore, cosine-like optical pulses (carrier-envelope phase of zero) lead to sine-like electron momentum modulation (carrier-envelope phase of $\pi/2$) and vice-versa. THz pulses from optical rectification typically have a carrier-envelope phase of zero in a focus [10,11] and therefore provide a sinusoidal momentum modulation. This time-dependency of Δp_z causes pulse compression by deceleration of the incoming pulse's earlier parts and acceleration of the later parts. Thus, only half an optical cycle is responsible for compression, and in case of pulses the relevant part of the momentum kick can be approximated by a modulation with a single frequency ω (see supplementary). If an incoming electron pulse is shorter than the optical half-cycle, we obtain isolated electron pulses [2], otherwise pulse trains [5,12]. The minimum pulse duration is achieved at the temporal focus $f_{temp} = \frac{\beta^2\gamma^3}{A_z E_0}\frac{m_e c^2}{e}$ (see supplementary); m_e is the electron mass and γ the Lorentz factor. Analogously, there is a time-dependent sideways deflection via $\Delta p_\mathrm{y} \propto A_\mathrm{y}$, which allows to realize a cathode ray oscilloscope at optical frequencies [2,5].

The geometry factors A_z and A_y are plotted in Fig. 1c and 1d for electrons with a kinetic energy of 70 keV. We find that there are certain combinations of angles for which $\Delta p_y = 0$, that is, no net deflection after interaction. This effect is due to cancelation of electric and magnetic contributions and occurs for $\sin\theta_{\mathrm{THz}} = \beta \sin\theta_{\mathrm{e}}$ and $\sin\theta_{\mathrm{THz}} = \beta^{-1} \sin\theta_{\mathrm{e}}$ (Fig. 1c-d, solid lines). For most other angular configurations, we find that deflection and acceleration occur simultaneously, providing opportunity for multi-dimensional control. The dotted lines mark a convenient region for pulse front tilting experiments, because the deflection is weak there and the compression strength is roughly constant when varying the slant angle of the mirror. The position of the temporal focus is therefore approximately independent of angular adjustments.

For electron beams with a finite diameter, certain angular configurations provide velocity-matching [9], that is, all electrons have the same relative delay to the optical cycles regardless of their position within the beam (Fig. 1b). Velocity matching is achieved if

$$\frac{c}{\sin\theta_{\mathrm{THz}}} = \frac{v_e}{\sin\theta_{\mathrm{e}}}, \qquad (4)$$

that is, if the superluminal phase velocity of the optical interference pattern along the mirror surface equals the surface velocity of the electron pulse's point of incidence. In order to generate tilted electron pulses, we rotate the mirror away from this velocity matching condition. This simple adjustment produces a lateral timing mismatch $\Delta T = \Delta t_{\mathrm{THz}} - \Delta t_e$ between the optical cycles and electrons of different beam positions ΔY (Fig. 1b). Considering the geometry depicted in Fig. 1b, we obtain

$$\frac{\Delta T}{\Delta Y} = \frac{\sin\theta_{\mathrm{THz}}/c - \sin\theta_{\mathrm{e}}/v_e}{\cos\theta_{\mathrm{e}}}. \qquad (5)$$

If the position-dependent delay is smaller than a half-period of the optical radiation, the momentum modulation is nearly linear in space and time. Therefore, incoming electron pulses obtain a position-dependent overall acceleration or deceleration in addition to the time-dependent longitudinal momentum modulation that causes compression. Consequently, there is a linear velocity gradient along the transverse beam profile (Fig. 1a) and different slices of the beam profile arrive earlier or later at the target, that is, as tilted pulses. The lateral arrival time difference of $\delta t/\delta y$ result in a tilt angle $\alpha = \tan^{-1}(v_\mathrm{e}\delta t/\delta y)$ for a collimated beam (Fig. 1a). At the temporal focus, we find $\delta t/\delta y = \Delta T/\Delta Y$ (see supplementary) and thus

$$\tan\alpha = v_\mathrm{e}\frac{\Delta T}{\Delta Y}. \qquad (6)$$

We see that the tilt angle in the temporal focus is solely determined by the combined sweeping dynamics of the electrons and the THz cycles across the mirror and does not dependent on the applied optical field strength or its wavelength. According to Eq. 6, compressed electron pulses can be produced at almost arbitrary tilt angle α and position f_temp, simply by rotating the mirror for the tilt and adjusting the optical field strength for the temporal focus position.

In the experiment, we use single-cycle THz pulses (central frequency 0.3 THz [10]) as control fields. The mirror element is a 10-nm Al-layer on a 10-nm SiN membrane (size 1.5×1.5 mm^2) with a reflectivity of >90% [13]. The transmission of our 70-keV electron pulses [14] is ~70%. Space charge effects are avoided by using <5 electrons per pulse [15] at a repetition rate of 50 kHz. We let the THz beam cross the electron beam approximately at 90° (see Fig. 1a). Finite transverse beam size effects of the electromagnetic wave can be neglected, because the electron beam diameter (<1 mm) is much smaller than w_0 (~3 mm) or z_R (~2 cm) of the THz pulses. The incident peak electric field strength is ~2×10^5 V/m which produces a temporal focus at $f_\mathrm{temp} \approx 0.5$ m and compresses the electron pulses from 1 ps to ~100 fs. For pulse tilt characterization, we use a magnetic solenoid lens that creates an intermediate waist (Fig. 1a, lower panel) and therefore a shadow image of the mirror on the screen (green). The half-angle divergence of the electron beam at the mirror is ~1 mrad. A butterfly-shaped metal resonator (orange) is placed at the waist position, which coincides with the temporal focus. It is illuminated with a second THz pulse [11] at ~9×10^5 V/m peak field strength and serves as a streaking element, that is, it deflects the electrons along the x-axis (out of the plane in Fig. 1a) as a function of arrival time [2]. This streaking metrology in combination with the shadow imaging allows to determine the arrival time differences δt between different parts of the beam profile along y, in order to measure the pulse front tilt of a collimated beam (Fig. 1a, upper panel).

Figure 2a shows raw screen images (each at a zero-crossing of the streaking field) for different slant angles of the mirror. The apparent shear in the data directly demonstrates the predicted arrival time differences between electrons originating from different points of the foil (dashed lines) and thus shows that tilted electron pulses are produced.

A quantitative analysis is obtained by recording a series of screen images while scanning the streaking delay (for details see Supplementary). This metrology reveals a time-dependent streaking trace for each position *y* in the electron beam (Fig. 2b). We see that each slice of the beam deflects with a sinusoidal dependency in time, following the half-cycle of the THz streaking field with a position-dependent delay (see inset). The slope of this measured delay is $\delta t/\delta y$ for the chosen mirror angle ($\theta_\mathrm{e} = 11.3°$ in the figure). Repetition of this procedure for all angles provides the blue dots in Fig. 2c, showing the measured lateral arrival time differences $\delta t/\delta y$ as a function of θ_e and θ_THz.

In a second, independent experiment we determine the relative strength of the transverse momentum kick Δp_y as a function of the mirror angle. To this end, the streaking element is removed and beam position changes are recorded as a function of the THz delay at the mirror. An aperture close to the foil (diameter 50 μm) decreases the beam diameter and a peak field strength of ~4×10^5 V/m further enhances the resolution. Figure 2d shows a subset of the measured deflectograms [2] as a function of the mirror angle. The observed time-dependent deflections are proportional to $\Delta p_\mathrm{y}(t)$. We see that all traces are single-cycle and sine-like, as expected from our cosine-like THz pulses [10] via the considerations above. The peak-to-peak amplitude is proportional to the geometry factor A_y for sideways momentum transfer and shows a strong dependency on the mirror slant angle (red dots in Fig. 2c). A least-squares fit to the data with Eq. 2 reveals the precise angle $\Delta\theta = \theta_\mathrm{THz} + \theta_\mathrm{e}$ between the electrons and the THz beam in the experiment, as well as a proportionality constant C that includes the camera distance and electric peak field strength. We obtain $\Delta\theta = (93.4 \pm 0.8)°$. The result is plotted as red solid line in Fig. 3c, which compares very well to the measured data and confirms the validity of the analytical expressions for sideways deflection (Eqs. 1-2). Using $\Delta\theta$, we compare the measured tilt parameters $\delta t/\delta y$ (blue dots) to $\Delta T/\Delta Y$ via Eq. 5 (blue solid line). We observe a good agreement; deviations at larger angles are attributed to residual shifts of the temporal focus by non-constant $\Delta p_z(\theta_e, \theta_{THz})$, which is neglected here (see Fig. 1c, dotted line). The agreement of the measured tilt data to the theory shows that tilted electron pulses are generated as predicted by Eq. 6.

The two separate experiments on tilt and deflection (blue and red data in Fig. 2c, respectively) reveal a non-trivial coincidence between the velocity-matching condition and absent deflection. Both data traces cross zero at the same angle θ_e^0, which happens to be the velocity matching angle according to Eq. 4. It follows that planar elements, if oriented according to Eq. 4, allow compressing electron pulses of arbitrarily large beam diameter by means of all-optical control without any unwanted time-dependent deflections.

Furthermore, we see from Fig. 2c that the measured pulse front tilt appears to be linked to the measured deflection strength: larger tilt angles imply stronger sideways effects. In optics, there is a direct relationship between pulse front tilt and angular dispersion via $\tan\alpha = \bar{\lambda}\, d\epsilon/d\lambda$ [16], where α is the pulse front tilt, $\bar{\lambda}$ is the spectral mean and $d\epsilon/d\lambda$ is the angular dispersion (change of deflection angle ϵ per wavelength λ). Our two experiments reveal a similar relation for electrons. We define the angular electron dispersion analogously to the optical case as $d\epsilon/d\lambda_{db}$, where ϵ is the electron deflection angle (Fig. 1b) and $\lambda_{db} \approx h/p_z$ is the electron de Broglie wavelength. In order to evaluate $d\epsilon/d\lambda_{db}$ from the data, we assume $p_y \ll p_z$ (paraxial approximation) and constant angular dispersion. Differentiating $\epsilon = p_y/p_z$ and λ_{db} yields $d\epsilon = \frac{1}{p_z}\left(dp_y - \frac{p_y}{p_z}dp_z\right)$, $d\lambda_{db} = -\lambda_{db}\frac{1}{p_z}dp_z$ and $\frac{d\epsilon}{d\lambda_{db}} = -\frac{1}{\lambda_{db}}\left(\frac{dp_y}{dp_z} - \frac{p_y}{p_z}\right)$. For $\lambda_{db} = \lambda_{db}^0$, where λ_{db}^0 is the initial de Broglie wavelength of the not-deflected electron ($\epsilon = 0$), we obtain $-\lambda_{db}^0\frac{d\epsilon}{d\lambda_{db}} = \frac{\Delta p_y}{\Delta p_z} = \frac{A_y(\theta_e,\theta_{THz})}{A_z(\theta_e,\theta_{THz})}$. A_y is obtained from the measured deflection amplitude (red dots in Fig. 3b) and A_z is calculated via Eq. 3 by using $\Delta\theta$ and C from the calibration of the setup.

The result of this conversion is reported in Fig. 3a, where we plot $\lambda_{db}^0\frac{d\epsilon}{d\lambda_{db}}$ (evaluated angular dispersion) against $\tan\alpha$ (measured tilt strength). We see that all data points are close to a straight line with a slope of unity (magenta). This experimental finding motivates the conjecture

$$\tan\alpha = \lambda_{db}^0\frac{d\epsilon}{d\lambda_{db}} \qquad (7)$$

for electron pulses in a temporal focus, where all energy components overlap in space and time. Equation 7 is the matter wave analogue to its optical counterpart [16].

In contrast to laser pulses, our electron pulses in the experiment have a 10^5 times shorter wavelength, a rest mass and sub-light speed. The beam is also rather incoherent and the electrons behave almost like point particles due to their low degree of coherence of $\sim 10^{-4}$ in space and $\sim 10^{-2}$ in time [15]. Furthermore, our way of generating tilted electron pulses is different from the optical approach, namely by applying a position-dependent acceleration/deceleration instead of using a passive dispersive element like a prism or a grating. The fact that there is nevertheless an apparent connection between tilt and dispersion in the experiment (see Fig. 3a) suggests that Eq. 7 might be general for any type of matter wave at arbitrary degree of coherence.

A simulation of a fully coherent electron wavepacket with a transverse momentum modulation is depicted in Fig. 3b, motivated by recent experimental advances in laser-triggered high-coherence electron sources [17]. We assume an initial electron wave function $\psi(y,z) = \exp\left[-z^2/\left(2{z_0}^2\right) - y^2/\left(2{y_0}^2\right) + i(k_0 + c_y y)z + ic_z z^2\right]$, where z_0 is the pulse length, y_0 is the wave packet width, k_0 is the mean wave vector, c_z is the chirp coefficient and c_y is a y-dependent longitudinal momentum change. Free-space propagation in a non-relativistic approximation is calculated via Fourier transformation, multiplication with the propagator $\exp[i\hbar k^2 t/(2m_e)]$ and back-transformation; t is the propagation time and k is the electron wave vector. We see (Fig. 3b) that the phase fronts are angled to the pulse shape, and different wavelengths travel at different angles (black circles). These simulations support Eq. 7 for the case of fully coherent electron wave packets.

In conclusion, our results show that tilted and compressed electrons pulses can efficiently be generated by all-optical means and simple interaction elements. Tilted electron pulses allow for ultrafast pump-probe diffraction and microscopy in which the optical cycles are used for sample excitation or control (see Fig. 4). In experiments where the electron pulses are longer than an optical period [4,5,12], the energy sidebands [4,9] will be coupled to the deflection angles [2,5], potentially enabling novel imaging concepts in electron microscopy [4,18]. Tailored optical control fields or interaction elements provide opportunity for complex phase space manipulations to create exotic beams and pulse shapes at target. We predict that the controlled generation of such electron pulses will enable a wide range of future applications in probing and controlling materials, possibly along with electron vortices, Airy or Bessel beams [19-22].

Acknowledgements

This work was supported by the European Research Council, the Munich-Centre for Advanced Photonics. We thank Ferenc Krausz for support and Kathrin Mohler for discussions.

Figure captions

Fig. 1. All-optical generation of tilted electron pulses. (a) Concept and experiment. Electron pulses (blue) pass through a mirror (dark grey) that is irradiated by single-cycle THz radiation (red). A travelling interference pattern along the mirror surface converts the electrons into compressed and tilted pulses. Lower panel: if the electron beam is focused with the magnetic lens, the tilt angle increases with decreasing beam size, with opposite sign after its waist. A THz-driven resonator (orange) and a phosphor screen (green) provide the necessary metrology to reveal this tilting dynamics by experiment. (b) Definition of angles for the analytical derivations. (c) Amplitude of the longitudinal momentum change as a function of the geometry. (d) Amplitude of the transverse momentum change. Dotted lines, angle combinations applied in the experiments; solid lines, zero-deflection conditions.

Fig. 2. Experimental results on tilted electron pulses. (a) Screen images for different mirror slant angles at the zero crossing of the streaking field. Scale bar, 1 mm. The pulse front tilt is evident from the measured lateral arrival time differences (dashed line, time axis). (b) Streaking traces (dots and diamonds) for different y-positions within the beam profile and sinusoidal fitting curves (solid). Inset, time-zero of the streaking traces. (c) Measured arrival time difference (blue dots) and deflection amplitude (red dots). Red line, fit by Eq. 2; squares are excluded. Blue line, prediction by Eq. 5. Error bars indicate one standard deviation. (d) Time-dependent deflection measurements (deflectograms) for different mirror slant angles.

Fig. 3. Pulse front tilt vs. angular dispersion for electrons, and quantum simulations. (a) Measured angular dispersion in electron pulses as a function of tilt angle (blue) in comparison to this work's conjecture (Eq. 7, magenta). Error bars indicate one standard deviation and are omitted when smaller than a data point. Unequal scanning ranges of the raw data (Fig. 2c) are accounted for by linear interpolation. (b) Quantum simulation of an electron wavepacket $\psi(z, y, t)$ with initial position-momentum correlation (left) propagated to the temporal focus f_{temp} (right). We assume a coherence time of 8 fs, a beam waist of 20 nm and a linear transverse change of forward momentum, as from the

experiment (black arrows). The electron energy is 1 eV, in order to make the de Broglie wavelength visible in the results. The phase fronts remain approximately perpendicular to the propagation direction, but the envelope becomes tilted. Angular dispersion is indicated by the black circles and constant throughout the simulation.

Fig. 4. Potential applications of tilted electron pulses. (a) Sub-cycle/attosecond electron diffraction [5]. A crystalline sample (green) is oriented along a zone axis for generating multiple Bragg spots. The laser phase front (violet) has a polarization along the crystal surface. Tilted electron pulses (blue) propagate with sub-light speed, but probe the sample in synchrony with the field cycles. (b) Sub-cycle low-energy electron diffraction (LEED). Laser cycles (violet) illuminate a sample material (green) at an angle due to practical space restrictions [23]. Tilted electron pulses (blue) can probe every part of the surface with the same delay with respect to the field cycles. (c) Sub-cycle electron microscopy. A transmission electron microscopy grid (TEM grid) can usually not be tilted a lot with respect to the twin lens in a high-resolution microscope. Nevertheless, a combination of tilted electron pulses (blue) and diagonal laser incidence (violet) can provide a uniform sub-cycle-level delay over the entire illuminated TEM grid area.

References

[1] E. A. Nanni, W. R. Huang, K.-H. Hong, K. Ravi, A. Fallahi, G. Moriena, R. J. D. Miller, and F. X. Kaertner. Terahertz-driven linear electron acceleration. *Nature Communications*, 6, OCT 2015.

[2] C. Kealhofer, W. Schneider, D. Ehberger, A. Ryabov, F. Krausz, and P. Baum. All-optical control and metrology of electron pulses. *Science*, 352(6284):429–433, April 2016.

[3] E. Curry, S. Fabbri, J. Maxson, P. Musumeci, and A. Gover. Meter-scale terahertz-driven acceleration of a relativistic beam. *Phys. Rev. Lett.*, 120(9):094801–, February 2018.

[4] B. Barwick, D. J. Flannigan, and A. H. Zewail. Photon-induced near-field electron microscopy. *Nature*, 462(7275):902–906, December 2009.

[5] Y. Morimoto and P. Baum. Diffraction and microscopy with attosecond electron pulse trains. *Nature Physics, doi 10.1038/s41567-017-0007-6*.

[6] E. Prat, F. Lohl, and S. Reiche. Efficient generation of short and high-power x-ray free-electron-laser pulses based on superradiance with a transversely tilted beam. *Physical Review Special Topics-accelerators and Beams*, 18(10):100701, October 2015.

[7] H. C. Shao and A. F. Starace. Detecting electron motion in atoms and molecules. *Physical Review Letters*, 105(26):263201, December 2010.

[8] V. S. Yakovlev, M. I. Stockman, F. Krausz, and P. Baum. Atomic-scale diffractive imaging of sub-cycle electron dynamics in condensed matter. *Scientific Reports*, 5:14581, September 2015.

[9] F. O. Kirchner, A. Gliserin, F. Krausz, and P. Baum. Laser streaking of free electrons at 25 keV. *Nature Photonics*, 8(1):52–57, January 2014.

[10] M. V. Tsarev, D. Ehberger, and P. Baum. High-average-power, intense THz pulses from a LiNbO3 slab with silicon output coupler. *Applied Physics B*, 122(2):1–5, 2016.

[11] W. Schneider, A. Ryabov, Cs. Lombosi, T. Metzger, Zs. Major, J. A. Fulop, and P. Baum. 800-fs, 330-uJ pulses from a 100-W regenerative Yb:YAG thin-disk amplifier at 300 kHz and THz generation in LiNbO3. *Optics Letters*, 39(23):6604–6607, December 2014.

[12] K. E. Priebe, C. Rathje, S. V. Yalunin, T. Hohage, A. Feist, S. Schäfer, and C. Ropers. Attosecond electron pulse trains and quantum state reconstruction in ultrafast transmission electron microscopy. *Nature Photonics*, 11:793–797, 2017.

[13] N. Laman and D. Grischkowsky. Terahertz conductivity of thin metal films. *Applied Physics Letters*, 93(5):051105, August 2008.

[14] L. Kasmi, D. Kreier, M. Bradler, E. Riedle, and P. Baum. Femtosecond single-electron pulses generated by two-photon photoemission close to the work function. *New Journal of Physics*, 17(3):033008, 2015.

[15] Peter Baum. On the physics of ultrashort single-electron pulses for time-resolved microscopy and diffraction. *Chemical Physics*, 423:55–61, September 2013.

[16] J. Hebling. Derivation of the pulse front tilt caused by angular dispersion. *Optical and Quantum Electronics*, 28(12):1759–1763, December 1996.

[17] D. Ehberger, J. Hammer, M. Eisele, M. Krüger, J. Noe, A. Högele, and P. Hommelhoff. Highly coherent electron beam from a laser-triggered tungsten needle tip. *Physical Review Letters*, 114(22):227601, June 2015.

[18] A. Ryabov and P. Baum. Electron microscopy of electromagnetic waveforms. *Science*, 353(6297):374–377, July 2016.

[19] J. Verbeeck, H. Tian, and P. Schattschneider. Production and application of electron vortex beams. *Nature*, 467(7313):301–304, September 2010.

[20] N. Voloch-Bloch, Y. Lereah, Y. Lilach, A. Gover, and A. Arie. Generation of electron airy beams. *Nature*, 494(7437):331–335, February 2013.

[21] V. Grillo, E. Karimi, G. C. Gazzadi, S. Frabboni, M. R. Dennis, and R. W. Boyd. Generation of nondiffracting electron Bessel beams. *Physical Review X*, 4(1):011013, January 2014.

[22] C. L. Zheng, T. C. Petersen, H. Kirmse, W. Neumann, M. J. Morgan, and J. Etheridge. Axicon lens for electrons using a magnetic vortex: The efficient generation of a Bessel beam. *Physical Review Letters*, 119(17):174801, October 2017.

[23] M. Gulde, S. Schweda, G. Storeck, M. Maiti, H. K. Yu, A. M. Wodtke, S. Schäfer, and C. Ropers. Ultrafast low-energy electron diffraction in transmission resolves polymer/graphene superstructure dynamics. *Science*, 345(6193):200–204, July 2014.

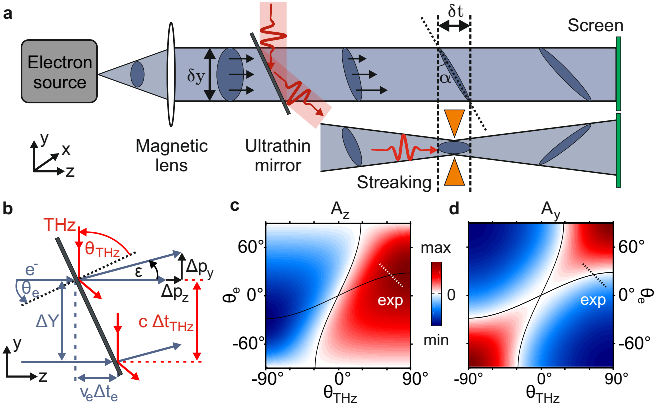
a
Electron source
Magnetic lens
Ultrathin mirror
δy
δt
α
Screen
Streaking
y
x
z
b
THz
θ_THz
ε
Δp_y
Δp_z
e⁻
θ_e
ΔY
c Δt_THz
v_eΔt_e
y
z
c
A_z
60°
0°
-60°
-90°
0°
90°
θ_e
θ_THz
exp
max
0
min
d
A_y
60°
0°
-60°
-90°
0°
90°
θ_e
θ_THz
exp

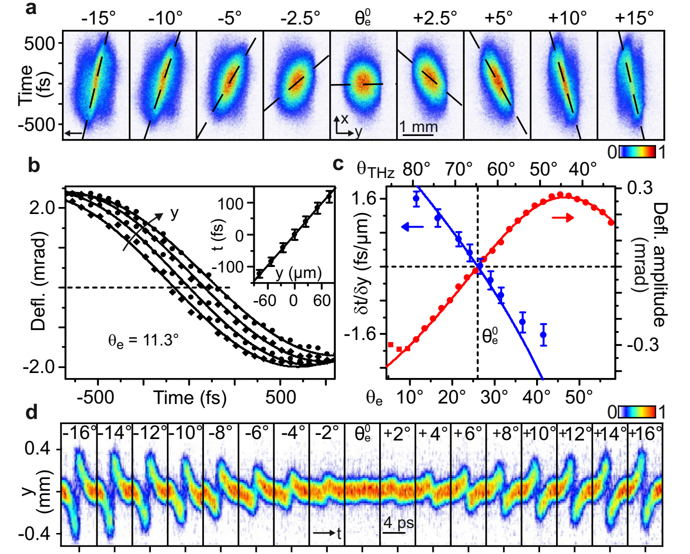

a
-15°
-10°
-5°
-2.5°
θ_e^0
+2.5°
+5°
+10°
+15°
Time (fs)
500
-500
x
y
1 mm
0
1
b
2.0
-2.0
Defl. (mrad)
y
θ_e = 11.3°
-500
Time (fs)
500
t (fs)
100
0
-100
y (μm)
-60
0
60
c
θ_{THz}
80°
70°
60°
50°
40°
1.6
-1.6
δt/δy (fs/μm)
0.3
-0.3
Defl. amplitude (mrad)
θ_e^0
θ_e
10°
20°
30°
40°
50°
d
0
1
-16°
-14°
-12°
-10°
-8°
-6°
-4°
-2°
θ_e^0
+2°
+4°
+6°
+8°
+10°
+12°
+14°
+16°
0.4
-0.4
y (mm)
t
4 ps

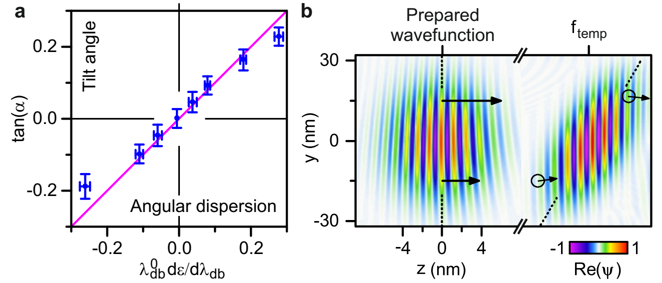

a
tan(α)
0.2
0.0
-0.2
Tilt angle
Angular dispersion
-0.2
0.0
0.2
$\lambda_{db}^{0} d\varepsilon/d\lambda_{db}$
b
Prepared wavefunction
f_{temp}
y (nm)
30
0
-30
-4
0
4
z (nm)
-1
1
Re(ψ)

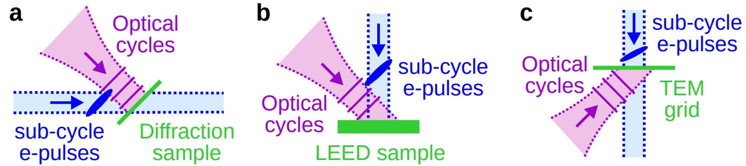
a
Optical
cycles
sub-cycle
e-pulses
Diffraction
sample
b
sub-cycle
e-pulses
Optical
cycles
LEED sample
c
sub-cycle
e-pulses
Optical
cycles
TEM
grid

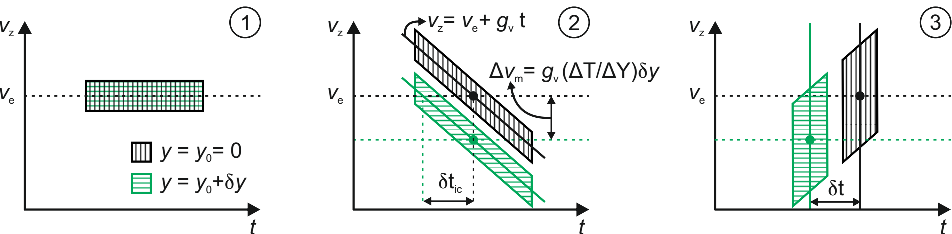

1
v_z
v_e
t
$y = y_0 = 0$
$y = y_0 + \delta y$
2
$v_z = v_e + g_v t$
$\Delta v_m = g_v (\Delta T/\Delta Y) \delta y$
v_z
v_e
δt_{ic}
t
3
v_z
v_e
δt
t